

This is the accepted manuscript made available via CHORUS. The article has been published as:

Electronic properties of epitaxial $\text{La}_{1-x}\text{Sr}_x\text{RhO}_3$ thin films

Juan Jiang, Alex Taekyung Lee, Sangjae Lee, Claudia Lau, Min Li, Tor M. Pedersen, Chong Liu, Sergey Gorovikov, Sergey Zhdanovich, Andrea Damascelli, Ke Zou, Frederick J.

Walker, Sohrab Ismail-Beigi, and Charles H. Ahn

Phys. Rev. B **103**, 195153 — Published 25 May 2021

DOI: [10.1103/PhysRevB.103.195153](https://doi.org/10.1103/PhysRevB.103.195153)

Electronic properties of epitaxial $\text{La}_{1-x}\text{Sr}_x\text{RhO}_3$ thin films

Juan Jiang^{1*}†, Alex Taekyung Lee^{1*}, Sangjae Lee², Claudia Lau², Min Li³, Tor M. Pedersen⁴, Chong Liu^{5,6}, Sergey Gorovikov⁴, Sergey Zhdanovich^{5,6}, Andrea Damascelli^{5,6}, Ke Zou^{5,6}, Frederick J. Walker¹, Sohrab Ismail-Beigi¹, and Charles H. Ahn^{1,2}

¹*Department of Applied Physics, Yale University, New Haven, Connecticut 06511, USA*

²*Department of Physics, Yale University, New Haven, Connecticut 06511, USA*

³*Materials Characterization Core, Yale West Campus, West Haven, Connecticut 06516, United States*

⁴*Canadian Light Source, Inc. 44 Innovation Boulevard, Saskatoon, SK S7N 2V3, Canada*

⁵*Department of Physics & Astronomy, University of British Columbia, Vancouver, BC V6T 1Z1, Canada*

⁶*Quantum Matter Institute, University of British Columbia, Vancouver, BC V6T 1Z4, Canada*

**These authors contribute equally to this work.*

† jjiangcindy@gmail.com

Abstract:

We report on the synthesis and electronic properties of epitaxial perovskite $\text{La}_{1-x}\text{Sr}_x\text{RhO}_3$ thin films. Thin films with a Sr content ranging from $x = 0$ to $x = 0.5$ have been grown using molecular beam epitaxy. Transport and x-ray photoemission spectroscopy data reveal an insulator-metal-insulator transition, accompanied by a p- to n- type carrier change observed in Hall measurements. Combined with theoretical calculations, we find that the addition of Sr does not directly dope carriers into the conduction band, but rather induces localized Rh 4d states within the LaRhO_3 band gap. The bandwidth of the impurity band increases with Sr content, eventually causing the valence band and the localized Rh 4d band to overlap, which explains the first insulator-to-metal transition occurring at $x = 0.35$. For Sr content $x > 0.4$, possible cation ordering results in an increase of the gap between the valence band and the Rh 4d band, leading to the second metal-to-insulator transition. We map out the electronic phase diagram of the Sr-doped LaRhO_3 system, and suggest strategies to engineer the electronic states in rhodates system via delocalizing the Rh^{3+} states.

Introduction:

Metal-to-insulator transitions (MIT) in transition metal oxides (TMO's) can be viewed as a quantum critical point where various physical phenomena are realized via tuning parameters such as doping, strain and pressure [1, 2]. Mechanisms for MITs induced by chemical substitution include Anderson localization

[3, 4], which is related to disorder in the electrostatic potential seen by the carriers, a Mott transition, which is related to electron correlations [5, 6], and charge disproportion, which is due to the existence of mixed valence states [7, 8]. The combination of two different MIT mechanisms have been observed in the well-studied 3d TMOs, such as $\text{La}_{1-x}\text{Sr}_x\text{MnO}_3$ [9-12], $\text{La}_{0.75}\text{Sr}_{0.25}\text{VO}_3$ [13], $\text{SrTi}_{1-x}\text{Ru}_x\text{O}_3$ [14-16], and the less-studied 4d Rh based TMO $\text{Sr}_{2-x}\text{La}_x\text{RhO}_4$ [17]. 4d TMO SrRhO_3 is interesting because it has been predicted to lie near a quantum critical point [18] and it is a candidate for topologically protected states, which can be realized by deliberately designing rhodium-based superlattices [19]. Moreover, due to its electronic configuration, rhodium-based double perovskites have been predicted to host unusual electronic and magnetic properties, such as ferromagnetic half metallic states in Cr-Rh and Mn-Rh compounds and antiferromagnetic states in Fe-Rh compounds [20]. However, due to the challenges in preparing a single-crystalline phase of rhodates, measurements of their properties are lacking. Polycrystalline samples of $\text{La}_{1-x}\text{M}_x\text{RhO}_3$ (M=Ca, Sr and Ba) have been studied, which exhibit a paramagnetic behavior [21] and a semiconducting to metal transition, which occurs at $x=0.3$ in $\text{La}_{1-x}\text{Sr}_x\text{RhO}_3$ systems [22]. Synthesis of SrRhO_3 thin films has been done with the pulsed laser deposition technique, where a C- type anti-ferromagnetic ground state, distinct from the bulk paramagnetic metallic ground state, is observed due to a modification of octahedral rotations by the substrate [23]. As a 4d TMO system with moderate electron correlation strength and moderate SOC, one might expect to observe new electronic states in rhodate thin films, starting with the perovskite band insulator LaRhO_3 (LRO), and modifying its electronic states using A-site substitution and epitaxial strain.

Here, we report the growth of $\text{La}_{1-x}\text{Sr}_x\text{RhO}_3$ ($x = 0\sim 0.5$) (LSRO) thin films on LaAlO_3 (001) (LAO) and SrTiO_3 (001) (STO) substrates by molecular beam epitaxy (MBE). *In-situ* reflection high-energy electron diffraction (RHEED) and atomic force microscopy (AFM) confirm the high crystalline quality of the MBE-grown thin films. X-ray diffraction (XRD) and x-ray photoemission (XPS) results show the systematic change of lattice parameter due to Sr doping, consistent with increasing Sr occupation on the A-site. An insulator-metal-insulator transition is observed in the doping range from $x = 0$ to $x = 0.5$, where a first insulator-to-metal transition takes place at $x = 0.35$ and is accompanied by a carrier type change from p- to n-. Another unexpected MIT transition happens at $x = 0.45$ in which the carriers remain n type. Our theoretical calculations predict that both electron-electron interactions and SOC effects are necessary to understand the electronic structure. The addition of Sr leads to the formation of an impurity state in the $\text{La}_{1-x}\text{Sr}_x\text{RhO}_3$ thin films, consisting of localized holes on Rh sites. As the Sr content is increased, the bandwidth of the impurity state increases to a point where it overlaps with the valence band and induces a metallic state.

Experimental and Theoretical Methods:

High quality Single crystalline LSRO thin films on both LAO (001) and STO (001) substrates are grown in an oxygen plasma assisted MBE system with a base pressure of $\sim 1 \times 10^{-10}$ Torr. The substrates are pre-annealed under O_2 plasma with a base pressure of 5×10^{-6} Torr at 500°C for half an hour to achieve clean surfaces. The La, Sr, Rh metals are co-deposited in an oxygen environment with an oxygen partial pressure of 3.5×10^{-6} Torr. The substrate temperature during growth is 700°C . The metal fluxes are calibrated using a quartz crystal microbalance to determine the relative stoichiometry prior to growth and to ensure a growth rate of 1 monolayer/minute. The film surface is monitored by *in-situ* RHEED during deposition. All films reported here are grown with 30 unit cell (uc) thickness with a typical thickness around 12 nm. To prevent the formation of oxygen vacancies, the samples are cooled down to room temperature under an oxygen plasma. The samples are characterized by using XRD, AFM, XPS, and a Quantum Design Physical Property Measurement System (PPMS). The XPS spectra are collected at room temperature using a monochromatic 1486.7 eV Al $K\alpha$ X-ray source and a PHI *VersaProbe* II X-ray Photoelectron Spectrometer with 0.47 eV resolution. The energy scale is calibrated using Cu $2p_{3/2}$ (932.67 eV) and Au $4f_{7/2}$ (84.00 eV) peaks on a clean copper plate and a clean gold foil. Synchrotron based valence band XPS is conducted on the Quantum Materials Spectroscopy Centre (QMSC) beamline at the Canadian Light Source at 10 K with a photon energy of 100 eV, with an energy resolution better than 15 meV. To avoid charging effects, the samples used for the synchrotron measurements are grown on Nb-doped STO substrates. Before the XPS measurements, the samples are annealed in 5×10^{-6} Torr oxygen plasma at 500°C for 2 hours.

For the theoretical calculations, we use the projector augmented wave method [24] as implemented in the Vienna *ab initio* simulation package software [25]. We use the revised version of the generalized gradient approximation (GGA) PBEsol, which is a revised Perdew-Burke-Ernzerhof GGA that improves equilibrium properties [26]. We also consider spin-orbit coupling self-consistently, where the spin quantization axis is the z-axis. The GGA with Hubbard U parameter, GGA+U scheme, within the rotationally invariant formalism [27] is used to improve the description of electronic interactions. The sizes of the supercells for $x = 0.0625$, 0.25, and 0.5 are 80, 20, and 20 atoms, respectively, corresponding to $2\sqrt{2} \times 2\sqrt{2} \times 2$, $\sqrt{2} \times \sqrt{2} \times 2$, and $\sqrt{2} \times \sqrt{2} \times 2$ unit cells, respectively. A plane wave basis with a kinetic energy cutoff 500 eV is used. $5 \times 5 \times 7$ ($x = 0.0625$) and $9 \times 9 \times 7$ ($x = 0.25$ and 0.5) k-point meshes are employed to sample the first Brillouin zone. The stress is relaxed only along the z-axis to be below $0.02 k_B$, while the in-plane lattice parameters are fixed to 3.905 \AA . We use $U(\text{Rh}) = 5 \text{ eV}$ to fit the optical energy gap of LaRhO_3 on STO substrates (1.3 eV) [28].

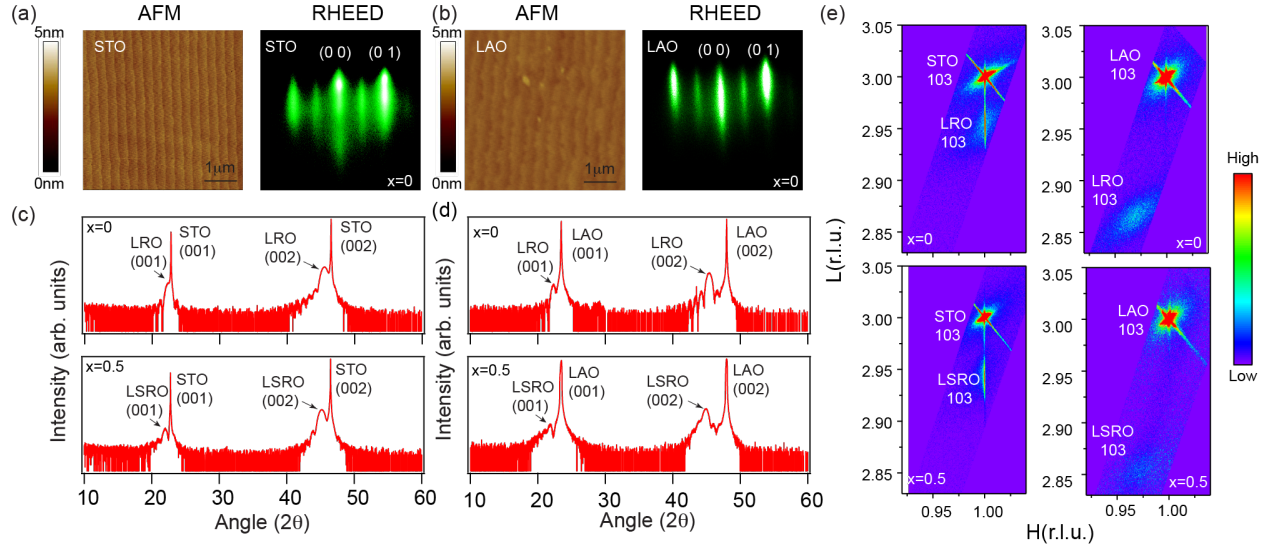


Figure 1. Characterization of LSRO films grown on STO and LAO substrates. (a) AFM topographic image (left) and RHEED pattern (right) of a 30-uc-thick LRO film on STO. (b) AFM topographic image (left) and RHEED pattern (right) of a 30-uc-thick LRO film on LAO. (c) XRD θ - 2θ scan of 30 uc LRO (top) and $x = 0.5$ (bottom) LSRO thin films on STO. (d) XRD θ - 2θ scan of 30 uc LRO (top) and $x = 0.5$ (bottom) LSRO thin films on LAO. (e) RSM around (103) reflections of $x = 0$ and $x = 0.5$ thin films on STO (left column) and on LAO (right column).

Results

The high crystallinity of the MBE-grown LSRO thin films is revealed by the AFM, RHEED, and XRD measurements in Fig.1. Topographic images and the RHEED patterns along the [100] directions of 30 uc thick LRO films grown on STO and LAO are shown in Fig.1(a) and Fig.1(b), respectively. Step terraces are visible in the AFM images with a single unit cell step height, with a root mean square root roughness less than 6 Å. The sharp and well-ordered RHEED patterns also indicate the growth of single crystalline epitaxial thin films. The phase purity is further confirmed by XRD measurements shown in Fig.1(c) and Fig.1(d) for $x=0$ and $x=0.5$ thin films grown on STO and LAO, respectively. The LSRO thin films covering the entire doping range ($x=0$ to 0.5) investigated here are grown under the same growth conditions, and all the thin films show comparable quality (See supplementary materials for the characterization data of the films). The out-of-plane lattice parameter, c , can be determined from the XRD θ - 2θ scan (Figs.1 (c, d)). We find that c increases from 3.98 Å ($x=0$) to 4.00 Å ($x=0.5$) on STO and from 3.98 Å ($x=0$) to 4.03 Å ($x=0.5$) on LAO with increasing Sr content, which is consistent with Sr replacing La in the perovskite structure. The reciprocal space maps (RSMs) around the substrate (103) reflections are performed on the samples. The results for $x=0$ and $x=0.5$ on both substrates are shown in Fig. 1(e). For the films grown on STO

substrates, the film peak and the substrate Bragg peak are aligned along the in-plane reciprocal space (H) direction, indicating that the film is coherently strained to the substrate. In contrast, for the films grown on LAO substrates, film peaks are well separated from the substrate peaks in both H and L directions, indicating the films are fully relaxed from the LAO substrate. The in-plane lattice parameter, a , can be determined from the RSM data to be 3.91\AA ($x=0$) and 3.89\AA ($x=0.5$) on LAO while for the thin films grown on STO the in-plane lattice constant is 3.905\AA through the entire doping range. The lattice constants a and c as a function of Sr concentration are displayed in the Supplementary Materials. From the similar lattice parameters for the films grown on LAO and STO, we expect to observe similar physical properties for the samples grown on the two substrates.

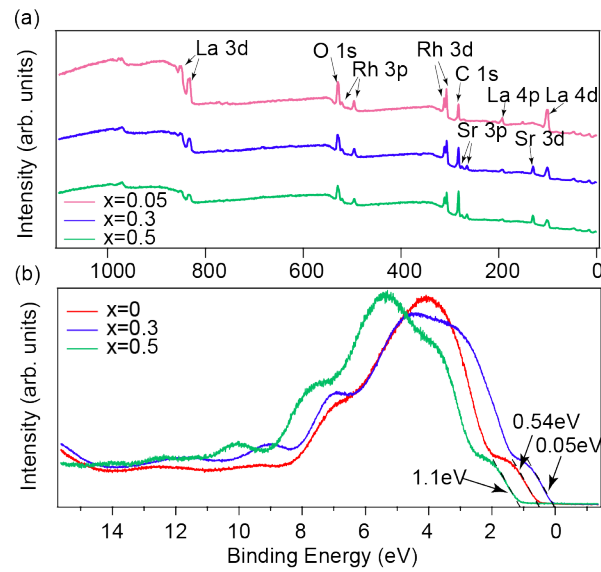


Figure 2. Photoemission measurements as a function of Sr content. (a) Wide energy range XPS data of $x=0.05$, $x=0.3$ and $x=0.5$ thin films. The characteristic core levels for La, Rh, Sr, and O are indicated. Note that a C $1s$ peak is also observed due to air exposure of the samples before the measurements. (b) Valence band XPS data of $x=0$, 0.3 and 0.5 LSRO films, which indicate a band gap of 0.54eV , 0.05eV and 1.1eV , respectively.

We perform XPS experiments to determine the chemical compositions of the thin films. Figure 2(a) presents XPS data for $x = 0.05$, $x = 0.3$ and $x = 0.5$ thin films. The characteristic peaks of all the elements are resolved (except for $x = 0.05$, where the Sr peak is too weak to be clearly resolved), and the peak ratio between La $3d$ and Sr $3d$ decreases, indicating the successful incorporation of Sr. The valence bands are measured with 100 eV photons after cleaning the sample under oxygen plasma (Fig. 2(b)). The LRO sample shows insulating behavior with an insulating band gap that is 0.54 eV , which is consistent with the band insulator behavior stemming from the $4d^6$ electronic configuration of LRO. As we dope Sr, the film becomes more metallic with a 0.05 eV band gap for $x = 0.3$. However, the $x = 0.5$ sample shows a band gap around 1.1eV according to the valence band XPS data, which is unexpected, since the electronic

configuration of Rh should be $4d^{5.5}$ and should result in a metallic phase in a simple band picture. **Note that the gap here determined from photoemission measurements is a gap between the valance band maximum and the Fermi level, which should be smaller than the insulating gap determined by the separation between the valence band top and the conduction band bottom; hence, we refer to this gap as δ .** However, the modulation of δ for different Sr doping should still reflect the information about the insulating band gap. Thus, a unique MIT transition with Sr doping is identified by the valence band XPS results; the origin of this unique MIT can be understood using first principles calculations discussed below.

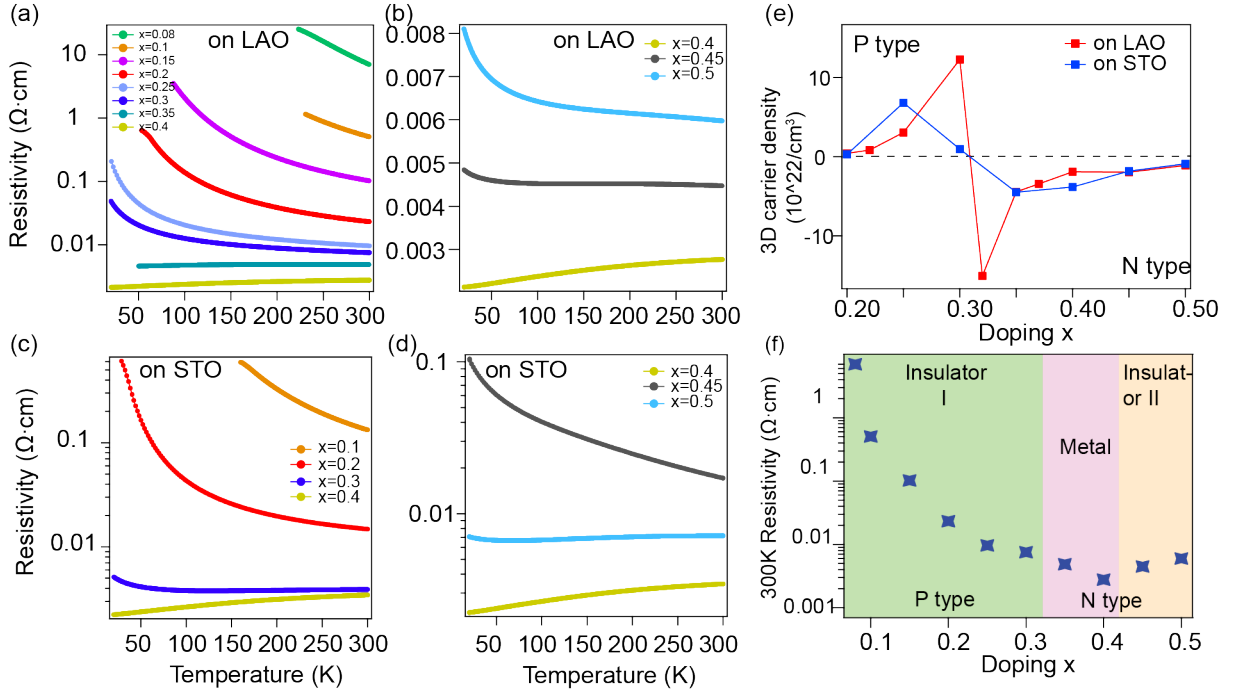


Figure 3. Temperature dependent resistivity (RT) as a function of Sr-doping. (a) RT curves of samples grown on LAO from $x = 0.08$ to $x = 0.4$. An insulator to metal transition occurs $x = 0.35$. (b) RT curves of samples grown on LAO from $x = 0.4$ to $x = 0.5$. A metal to insulator transition takes place at $x = 0.45$. (c) RT curves of samples grown on STO from $x = 0.08$ to $x = 0.4$. An insulator to metal transition occurs $x = 0.4$. (d) RT curves of samples grown on STO from $x = 0.4$ to $x = 0.5$. A metal to insulator transition takes place at $x = 0.45$. (e) 3D carrier densities of the LSRO thin films on both LAO and STO substrates. (f) Phase diagram of the LSRO thin films, showing the insulator-metal-insulator transition and a p type to n type carrier transition. The data plotted are extracted from the room temperature resistivity of the thin films grown on LAO.

To further interpret this unique MIT observed by valence band XPS, the temperature dependent resistivity (RT) of the LSRO thin films on both LAO and STO substrates are shown in Fig. 3 **(The LRO data is not shown since the sample is too insulating for transport measurements)**. For the LSRO samples on LAO, at lower doping ($x < 0.3$), the film is insulating, which is consistent with our results in Fig. 2(b). The

LSRO thin films start to be metallic above $x = 0.35$, reflecting the first MIT transition in the system. Interestingly, the electrical conductivity starts to decrease at $x = 0.45$, while the RT curve shows an insulating behavior again. This is consistent with the valence band XPS data of the $x = 0.5$ sample where an insulating gap of 1.1 eV is found. A similar phenomenon exists in the samples grown on STO as shown in Figs. 3(c, d). One may notice that the precise doping level for the MIT transition are slightly different for the films on two substrates, which may be due to the slight difference ($\sim 0.7\%$) in their lattice parameters.

In order to visualize which conduction channel contributes to this electronic transport behavior in LSRO thin films, we conduct room temperature Hall measurements of the samples, covering the entire doping range which can be investigated (Note that data of samples below $x=0.2$ are missing due to the fact that the sample is too insulating to be measured). The 3D carrier densities of the thin films deduced from the Hall data are summarized in Fig. 3(e) (The data below $x=0.2$ are missing due to the sample is too insulating for Hall measurements). The hole-type carriers dominate the charge transport in the lower doping range below $x = 0.3$. However, there is an abrupt transition from hole-type to electron-type carrier above $x = 0.3$ on both substrates, accompanied by an insulator-to-metal transition, and the carrier type remains electron-type for the higher doping ranges. The experimental observations on these transport measurements are summarized Fig. 3(f), where room temperature resistivity vs. Sr-doping, x , is plotted. In this phase diagram, we refer to the three different phases as insulator I, metal, and insulator II phases, respectively. In the insulator I phase, p-type carriers dominate the transport, while in the metal and insulator II phases n-type carriers dominate the transport. Using the formula relating Hall resistivity to carrier density in a single carrier model ($n=B/(R_H*q*d)$, where B is the magnetic field, R_H is the Hall resistance, q is the elementary charge, the sign of n is the carrier type, and d is the thickness of the film), one obtains an unphysical result that the effective carrier density diverges while approaching the first MIT. This means that at least two types of carriers (e.g., electrons and holes) must be considered. The unexpected change in the Hall carrier type indicates that an electronic transition may happen above $x = 0.3$, whereas the presence of the MIT within the electron carrier type regime cannot be understood without further electronic reconstruction around the Fermi level. The origin of this unique carrier type change and how the second exotic MIT transition is induced is further discussed below.

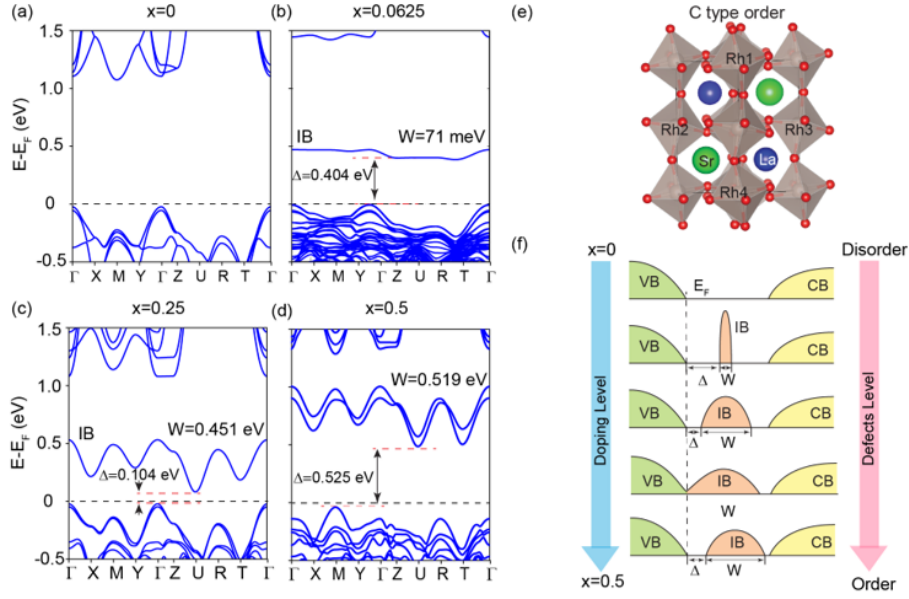


Figure 4. (a-d) Theoretical calculations of the band structures of $x = 0, 0.0625, 0.25$, and 0.5 LSRO thin films, respectively. (e) Schematic of a C-type ordering of the Sr and La cations. (f) Schematic of the change in band structures and electronic states with different doping levels.

Discussion

We conduct first principles calculations to better understand these MIT transitions at $x = 0.35$ and $x = 0.45$. The calculations are performed for ordered structures with $x = 0, 0.0625, 0.25$ and 0.5 , where unit cells with a a^-b^+ type octahedral tilt are used with sizes of $2\sqrt{2} \times 2\sqrt{2} \times 2$, $\sqrt{2} \times \sqrt{2} \times 2$, and $\sqrt{2} \times \sqrt{2} \times 2$, respectively (80, 20 and 20 atoms per cell). As shown in Figs. 4(a-d), adding Sr results in the formation of an impurity band (IB), which sits in between the valance band (VB) and conduction band (CB), instead of simply doping mobile holes into the system. This impurity band is composed of localized holes on Rh^{3+} sites. For a small Sr content, $x = 0.0065$, the IB is narrow with a bandwidth $W = 71$ meV, with negligible overlap between neighboring Rh^{3+} sites. The bandgap Δ which is determined by the distance between the VB top and the IB bottom is around 0.404 eV. Charge carriers are induced by thermal electron-hole excitation so that, at low Sr content, the more highly mobile holes in the valence band dominate the Hall resistance and the conduction is apparently p-type. Once the amount of dopant is increased, the bandwidth of the IB is increased to $W = 0.451$ eV for $x = 0.25$, and this results in a smaller bandgap $\Delta = 0.104$ eV. The increased hopping of electrons in the IB means that the electrons start to contribute to the Hall resistance, and the coexistence of both hole and electron transport causes an apparent increase in the 3D carrier concentration. This trend with Sr content is shown schematically in Fig. 4(f), which shows that for a Sr content of $x \sim 0.4$, the IB band bottom overlaps with the top of the VB, resulting in a metallic state which

occurs experimentally at $x = 0.35$. At this point the calculations suggest that the bandwidth of the IB is large enough that the Hall resistance changes signs and electrons become the dominant charge carrier.

The use of a small and ordered $\sqrt{2} \times \sqrt{2} \times 2$ unit cell containing only 4 Rh atoms (20 atoms total) for $x=0.25$ and 0.5 means that effects of disorder, e.g., Anderson localization, are not present in the calculations since the A site dopants are placed in an ordered manner. To study the qualitative effects of disorder, we consider random configurations of Sr atom dopants at $x=0.5$ in the $2\sqrt{2} \times 2\sqrt{2} \times 2$ unit cell containing 16 Rh atoms (80 atoms total). We compute the electronic spectra for five random configurations and confirm that LaRhO_3 is insulating with a clear band gap near the Fermi level for the five cases, indicating that the insulating properties are not due to Anderson localization but rather to the localization of holes (see Figs. S5 and S6).

The measured transport and valence band XPS data for $x = 0.5$ are explained qualitatively by a tendency of the Sr and La cations to order in a c-type configuration. (Fig. 4(e)). For a fully ordered structure, the band gap Δ increases dramatically to 0.525 eV, as shown in Fig. 4(d). This observation agrees with the experimental data, indicating that the ordering of the defects with doping may play a role in the reentrant transport behavior shown in Fig. 3(f). While we do not observe Bragg reflections in XRD due to c-type cation ordering, the tendency predicted by theory is enough to widen the energy gap. Indeed, the calculated band structure in Fig. 4(d) for $x = 0.5$ is not fully insulating, which may be due to only partial ordering of the cations. In addition, the band structure calculation qualitatively fits the valence band XPS measurements of the bandgap.

Summary

We find using a combination of theory and experiment that the addition of Sr to the band insulator LaRhO_3 adds localized Rh^{3+} bound states within the band gap. For small doping concentrations, a narrow impurity band forms and the system behaves as a standard p-type doped material. Higher levels of doping lead to a surprising change of carrier type to n-type, coincident with an insulator to metal transition: theory and experiment show this is due to the impurity band intersecting the valence band, as the former widens. Further Sr doping leads to another transition to a n-type insulator: theory suggests that at high doping levels, a structural ordering of the cations associated with a charge disproportionation among the Rh sites leads to an opening of a gap between the valence and the impurity band. These unexpected transitions point to the complex and interesting physics of the rhodate system. Future strategies for delocalizing the Rh^{3+} states that may lead to higher conductivity include structural modifications via substitution of other alkaline rare-earth cation dopants.

Acknowledgments

Work at Yale is supported by the U.S. Department of Energy (DOE), Offices of Science, Office of Basic Energy Sciences under Award No. DE-SC0019211. Synchrotron-based XPS measurements were performed at the Canadian Light Source, a national research facility of the University of Saskatchewan, which is supported by the Canada Foundation for Innovation (CFI), the Natural Sciences and Engineering Research Council (NSERC), the National Research Council (NRC), the Canadian Institutes of Health Research (CIHR), the Government of Saskatchewan, and the University of Saskatchewan. This research was undertaken thanks in part to funding from the Max Planck-UBC-UTokyo Centre for Quantum Materials and the Canada First Research Excellence Fund, Quantum Materials and Future Technologies Program. This project is also funded by the Canada Research Chairs Program (A.D.), and the CIFAR Quantum Materials Program (A.D.).

References:

- [1] M. Imada, A. Fujimori and Y. Tokura, Reviews of Modern Physics 70, 1039 (1998).
- [2] A. T. Lee and C. A. Marianetti, Physical Review B 97, 045102 (2018).
- [3] P. W. Anderson, Physical Review 109, 1492 (1958).
- [4] F. Evers and A. D. Mirlin, Reviews of Modern Physics 80, 1355 (2008).
- [5] A. Georges, G. Kotliar, W. Krauth and M.J. Rozenberg, Reviews of Modern Physics 68, 13 (1996).
- [6] N. F. Mott, Proceedings of the Physical Society. Section A 62, 416 (1949).
- [7] J. Cheng, K. E. Kweon, S. A. Larregola, Y. Ding, Y. Shirako, L. G. Marshall, Z. Y. Li, X. Li, A. M. dos Santos, M. R. Suchomel, K. Matsubayashi, Y. Uwatoko, G. S. Hwang, J. B. Goodenough and J. S. Zhou, Proc Natl Acad Sci USA 112, 1670 (2015).
- [8] S. Johnston, A. Mukherjee, I. Elfimov, M. Berciu and G.A. Sawatzky, Physical Review Letters 112, 106404 (2014).
- [9] A. Seeger, P. Lunkenheimer, J. Hemberger, A.A. Mukhin, V.Y. Ivanov, A.M. Balbashov and A. Loidl, Journal of Physics: Condensed Matter 11, 3273 (1999).
- [10] A. Urushibara, Y. Moritomo, T. Arima, A. Asamitsu, G. Kido and Y. Tokura, Physical Review B: Condensed Matter 51, 14103 (1995).
- [11] M. B. Salamon and M. Jaime, Reviews of Modern Physics 73, 583 (2001).
- [12] E. Dagotto, T. Hotta and A. Moreo, Physics Reports 344, 1 (2001).
- [13] T. M. Dao, P. S. Mondal, Y. Takamura, E. Arenholz and J. Lee, Applied Physics Letters 99, 112111 (2011).
- [14] K. W. Kim, J. S. Lee, T. W. Noh, S. R. Lee and K. Char, Physical Review B 71, 125104 (2005).
- [15] J. Kim, J. Y. Kim, B. G. Park and S. J. Oh, Physical Review B 73, 235109 (2006).
- [16] R. Gupta, I. N. Bhatti and A. K. Pramanik, Journal of Magnetism and Magnetic Materials 465, 193 (2018).
- [17] J. Kwon, M. Kim, D. Song, Y. Yoshida, J. Denlinger, W. Kyung and C. Kim, Physical Review Letters 123, 106401 (2019).
- [18] D. J. Singh, Physical Review B 67, 054507 (2003).
- [19] J.-M. Carter, V. V. Shankar, M. A. Zeb and H.-Y. Kee, Physical Review B 85, 115105 (2012).
- [20] A. Halder, D. Nafday, P. Sanyal and T. Saha-Dasgupta, npj Quantum Materials 3, 17 (2018).
- [21] T. Nakamura, T. Shimura, M. Itoh, and Y. Takeda, Journal of Solid State Chemistry 103, 523(1993).
- [22] T. A. Mary and V. Varadaraju, Journal of Solid State Chemistry 110, 176 (1994).
- [23] J. Nichols, S.F. Yuk, C. Sohn, H. Jeon, J.W. Freeland, V.R. Cooper and H.N. Lee, Physical Review B 95, 245121 (2017).
- [24] P. E. Blochl, Physical Review B: Condensed Matter 50, 17953 (1994).

[25] G. Kresse and D. Joubert, *Physical Review B* 59, 1758 (1999).

[26] J. P. Perdew, A. Ruzsinszky, G. I. Csonka, O. A. Vydrov, G. E. Scuseria, L. A. Constantin, X. Zhou and K. Burke, *Physical Review Letters* 100, 136406 (2008).

[27] A. I. Liechtenstein, V. V. Anisimov, J. Zaanen, *Physical Review B: Condensed Matter* 52, R5467 (1995).

[28] M. Nakamura, Y. Krockenberger, J. Fujioka, M. Kawasaki and Y. Tokura, *Applied Physics Letters* 106, 072103 (2015).

[1] M. Imada, A. Fujimori, Y. Tokura, Metal-insulator transitions, *Reviews of Modern Physics*, 70 (1998) 1039.

[2] A.T. Lee, C.A. Marianetti, Structural and metal-insulator transitions in rhenium-based double perovskites via orbital ordering, *Physical Review B*, 97 (2018).

[3] P.W. Anderson, Absence of Diffusion in Certain Random Lattices, *Physical Review*, 109 (1958) 1492-1505.

[4] F. Evers, A.D. Mirlin, Anderson transitions, *Reviews of Modern Physics*, 80 (2008) 1355-1417.

[5] A.G.G.K.W.K.a.M.J. Rozenberg, Dynamical mean-field theory of strongly correlated fermion systems and the limit of infinite dimensions, *Reviews of Modern Physics*, 68 (1996).

[6] <LaSrCoO3 Structure and Magnetism_Goodenough.pdf>, DOI.

[7] J. Cheng, K.E. Kweon, S.A. Larregola, Y. Ding, Y. Shirako, L.G. Marshall, Z.Y. Li, X. Li, A.M. dos Santos, M.R. Suchomel, K. Matsubayashi, Y. Uwatoko, G.S. Hwang, J.B. Goodenough, J.S. Zhou, Charge disproportionation and the pressure-induced insulator-metal transition in cubic perovskite PbCrO₃, *Proc Natl Acad Sci U S A*, 112 (2015) 1670-1674.

[8] S. Johnston, A. Mukherjee, I. Elfimov, M. Berciu, G.A. Sawatzky, Charge disproportionation without charge transfer in the rare-earth-element nickelates as a possible mechanism for the metal-insulator transition, *Phys Rev Lett*, 112 (2014) 106404.

[9] A. Seeger, P. Lunkenheimer, J. Hemberger, A.A. Mukhin, V.Y. Ivanov, A.M. Balbashov, A. Loidl, Charge carrier localization in La_{1-x}Sr_xMnO₃ investigated by ac conductivity measurements, *Journal of Physics: Condensed Matter*, 11 (1999) 3273-3290.

[10] A. Urushibara, Y. Moritomo, T. Arima, A. Asamitsu, G. Kido, Y. Tokura, Insulator-metal transition and giant magnetoresistance in La_{1-x}Sr_xMnO₃, *Phys Rev B Condens Matter*, 51 (1995) 14103-14109.

[11] M.B. Salamon, M. Jaime, The physics of manganites: Structure and transport, *Reviews of Modern Physics*, 73 (2001) 583.

[12] E. Dagotto, T. Hotta, A. Moreo, Colossal magnetoresistant materials: the key of the phase transition, *Physics Reports* 344 (2001) 1-153.

[13] T.M. Dao, P.S. Mondal, Y. Takamura, E. Arenholz, J. Lee, Metal-insulator transition in low dimensional La_{0.75}Sr_{0.25}VO₃ thin films, *Applied Physics Letters*, 99 (2011).

[14] K.W. Kim, J.S. Lee, T.W. Noh, S.R. Lee, K. Char, Metal-insulator transition in a disordered and correlated SrTi_{1-x}Ru_xO₃ system: Changes in transport properties, optical spectra, and electronic structure, *Physical Review B*, 71 (2005).

[15] J. Kim, J.Y. Kim, B.G. Park, S.J. Oh, Photoemission and x-ray absorption study of the electronic structure of SrRu_{1-x}Ti_xO₃, *Physical Review B*, 73 (2006).

[16] R. Gupta, I.N. Bhatti, A.K. Pramanik, Critical behavior in itinerant ferromagnet SrRu_{1-x}Ti_xO₃, *Journal of Magnetism and Magnetic Materials*, 465 (2018) 193-200.

- [17] J. Kwon, M. Kim, D. Song, Y. Yoshida, J. Denlinger, W. Kyung, C. Kim, Lifshitz-Transition-Driven Metal-Insulator Transition in Moderately Spin-Orbit-Coupled $\text{Sr}_{2-x}\text{La}_x\text{RhO}_4$, *Phys Rev Lett*, 123 (2019) 106401.
- [18] D.J. Singh, Prospects for quantum criticality in perovskite SrRhO_3 , *Physical Review B*, 67 (2003).
- [19] J.-M. Carter, V.V. Shankar, M.A. Zeb, H.-Y. Kee, Semimetal and Topological Insulator in Perovskite Iridates, *Physical Review B*, 85 (2012).
- [20] A. Halder, D. Nafday, P. Sanyal, T. Saha-Dasgupta, Computer predictions on Rh-based double perovskites with unusual electronic and magnetic properties, *npj Quantum Materials*, 3 (2018).
- [21] T.S. Tetsuro Nakamura, Mitsuru Itoh, and Yasuo Takeda, Magnetic and electric properties of $\text{La}_{1-x}\text{M}_x\text{RhO}_3$ (M=Ca, Sr, and Ba): hole doping of 4d orbitals of Rh^{3+} with low spin configuration *Journal of Solid State Chemistry* 103, 523, DOI (1993).
- [22] T.A.M.a.U.V. Varadaraju, Orthorombic to tetragonal and semiconductor-metal transitions in the $\text{La}_{1-x}\text{Sr}_x\text{RhO}_3$ system *Journal of Solid State Chemistry* 110, 176, DOI (1994).
- [23] J. Nichols, S.F. Yuk, C. Sohn, H. Jeon, J.W. Freeland, V.R. Cooper, H.N. Lee, Electronic and magnetic properties of epitaxial SrRhO_3 films, *Physical Review B*, 95 (2017).
- [24] P.E. Blochl, Projector augmented-wave method, *Phys Rev B Condens Matter*, 50 (1994) 17953-17979.
- [25] G. Kresse, D. Joubert, From ultrasoft pseudopotentials to the projector augmented-wave method, *physical Review B*, 59 (1999).
- [26] J.P. Perdew, A. Ruzsinszky, G.I. Csonka, O.A. Vydrov, G.E. Scuseria, L.A. Constantin, X. Zhou, K. Burke, Restoring the density-gradient expansion for exchange in solids and surfaces, *Phys Rev Lett*, 100 (2008) 136406.
- [27] A.I. Liechtenstein, V.V. Anisimov, J. Zaanen, Density-functional theory and strong interactions: Orbital ordering in Mott-Hubbard insulators, *Phys Rev B Condens Matter*, 52 (1995) R5467-R5470.
- [28] M. Nakamura, Y. Krockenberger, J. Fujioka, M. Kawasaki, Y. Tokura, Perovskite LaRhO_3 as a p-type active layer in oxide photovoltaics, *Applied Physics Letters*, 106 (2015) 072103.